Phase and morphology controllable synthesis of superhydrophobic Sb_2O_3 via a solvothermal method

Shiwen Zhu,[a]Xiaojuan Yang, [a]Taohai Li[a,*], Feng Li[a] and Wei Cao[b]

[a]*College of Chemistry, Key Lab of Environment Friendly Chemistry and Application in Ministry of Education, Xiangtan University, Xiangtan, 411105, China*

[b]*Nano and Molecular Systems Research Unit, Faculty of Science, P.O. Box 3000, University of Oulu, FIN-90014, Finland*

[*]Correspondence Author.Tel.: +86-731-58292202; fax: +86-731-8292251;

E-mail address: hnlth@xtu.edu.cn.(T. Li)

Abstract:

In this article, we report on a controllable synthesis of superhydrophobic Sb_2O_3 microcrystals via a solvothermal method assisted with the soluble inorganic Na_2WO_4 salt. Morphologies of the final products depend on the amount of the OH^- ions adsorbed on Sb_2O_3 nanoplates. By varying the amount of NaOH, the octahedral Sb_2O_3 can be switched to microcrystals or microspindles. Reaction and formation mechanisms of Sb_2O_3 were also proposed, which may also benefit synthesis of other metal oxides with controllable morphology. Additionally, after modified by (Heptadecafluoro-1,1,2,2-tetradecyl) trimethoxysilane, the as-synthesized octahedral Sb_2O_3 microcrystals and Sb_2O_3 microspindles show superhydrophobic and excellent anticorrosion properties in acidic and basic circumstances.

Keywords: Sb_2O_3; Solvothermal; Superhydrophobic; Water Adhesion

1. Introduction

Superhydrophobicity refers to surface with water static contact angles (SCAs) above 150° and sliding angles (SAs) below 10°. Due to its unique applications in self-cleaning [1-3], corrosion resistance [4-6], anti-icing [7,8] and drag-reduction [9], various investigations have been carried out to reach this special wettability. When a CA hysteresis is considered, the superhydrophobic surfaces often show five possible states: Wenzel's state, Cassie's state, the "lotus" state, the transitional state between Wenzel's and Cassie's states, and the "gecko" state. Among them, the Wenzel's state and Cassie's state are two classical models to explain the surface superhydrophobicity. The Wenzel's state applies to the not-so-rough surfaces on which water is repelled [10]. In this state, water droplets adhere to the superhydrophobic surface, even when the surface is turned upside down [11-13]. Such an adhesive but superhydrophobic surface attracts a lot of interests because of the promising potentials in droplet-based technologies [14-17]. Cassie's state, in contrast, dominates the wettability when the surface is extremely rough. In this state, the water droplet on solid surfaces is adopting a non-wet-contact mode and can roll off easily because of their low adhesive force [18, 19]. The "lotus" state exists on surfaces with strong repellency to water. Large CAs (>150^{o}) and small SAs (<5^{o}) are normally found [20]. It can be considered as a unique case of Cassie's state, because a lotus leaf exhibits the self-cleaning effect. Additionally, a transitional state between Wenzel's and

Cassie's states often exists when water droplets contact most practical samples. The water droplet can be hung, even after flipping the surface. A typical example can be visualized as the water droplets on a rose petal. Consequently, this special transition state is also called "petal" state [21]. Originated from the superhydrophobic surface of the PS nanotube [22], the high-adhesive "gecko" state is composed of air pockets trapped in the PS nanotubes, and open air pockets linked to the atmosphere. The trapped air results in a high CA, and the negative pressure from the sealed air in the nanotubes produces the adhesive force.

To reach surface hydrophobicity, coating materials with specific micro- to nano- structures are usually needed. As an important member of the main group metal oxides, antimony trioxide (Sb_2O_3) is widely used in several technological fields such as flame retardant paints, functional filler, adhesives, and textile [23]. It is also functional as a catalyst in the polyester industry and indirect-gap semiconductor material with extraordinary optoelectronic properties [24]. The surface morphology strongly affects materials properties. Recently, several synthesis methods have been reported to prepare Sb_2O_3 in morphologies of nanorods [25], nanotubes [26], and nanobelts [27]. These specific nanostructures may enable the practical application in superhydrophobic coatings. The synthesis was developed e.g., through micro emulsion method [28], chemical reducing method [29] and solution route [30]. Although synthesis of Sb_2O_3 by solvothermal method has been reported

[31-34], they are suffering from the addition of surfactant [31, 32], long reaction time [33], or the generation of poisonous gas [34]. Therefore, a simple and environmentally friendly method is desired for the synthesis of Sb_2O_3 with different morphologies.

In this work, morphology-controllable Sb_2O_3 nanostructures were fabricated by a facile solvothermal method. We obtained cubic-phased octahedra microcrystals and orthorhombic-phased microspindles at different synthesis pH values. Possible reaction and growth mechanisms of Sb_2O_3 were proposed. After modification of (Heptadecafluoro-1,1,2,2-tetradecyl) trimethoxysilane (PFOST), the as-synthesized octahedral Sb_2O_3 microcrystals and Sb_2O_3 microspindles turned to be superhydrophobic and anticorrosive in acidic and basic ambiences.

2. Materials and methods

2.1. Preparation of Sb_2O_3 microstructure

All of the reagents were analytical graded and used without further purification. In a typical procedure, 4 mmol $SbCl_3$ was dissolved in 8 ml ethanol solution and 2 mmol $Na_2WO_4 \cdot 2H_2O$ was dissolved in 8 mL distilled water, and both of them were stirred for 10 mins. After that, two solutions were mixed together to form homogeneous systems. A certain amount of NaOH solution was added to adjust the pH values of the solution from 9 to11. After 30 min stirring, the mixture was transferred into a Teflon-lined autoclave of 20 mL capacity. It was sealed and heated to 180 ^oC for 24 h, and then cooled down to

room temperature naturally. The white powders were collected, washed with deionized water and absolute alcohol for several times and then dried in vacuum at 60 °C for 12 h. Depending on the pH value of the precursor (9, 10, 11), the products with different morphologies can be synthesized and labelled as S9, S10 and S11, respectively.

To investigate the role of reaction time in the synthesis of Sb_2O_3, different reaction time was applied for the preparation of Sample S1 (pH=9, t=12h), S2 (pH=9, t=48h), S3 (pH=11, t=12h) and S4 (pH=11, t=48h). For comparison purpose, sample S5 (S6) were prepared under the same conditions as the sample S9 (S11) except for the adding of Na_2WO_4. The detailed conditions are tabulated in Table 1.

Table 1

samples	$SbCl_3$/g	$Na_2WO_4 \cdot 2H_2O$ /g	pH	reaction condition
S1	0.912	0.660	9	180°C, 12h
S2	0.912	0.660	9	180°C, 48h
S3	0.912	0.660	11	180°C, 12h
S4	0.912	0.660	11	180°C, 48h
S5	0.912	0	9	180°C, 24h
S6	0.912	0	11	180°C, 24h
S9	0.912	0.660	9	180°C, 24h
S10	0.912	0.660	10	180°C, 24h
S11	0.912	0.660	11	180°C, 24h

2.2. Characterization of Sb_2O_3

The crystalline structure of the as-prepared Sb_2O_3 powders were characterized by powder X-ray diffraction (XRD) with a Shimadzu Dmax γ A X-ray diffractometer, using monochromatized Cu-Kα (λ=0.15418 nm), and

scanning over the range of $20^{\circ} \leqslant 2\theta \leqslant 80^{\circ}$. The morphologies and microstructures characterizations were performed on the scanning electron microscopy (SEM, JEOL JSM-6700F). The contact angles (CAs) were measured through a dynamic CA analyzer (FTÅ 200, USA) at room temperature.

2.3. Wettability measurement

The contact angle (CA) was measured with an optical contact angle meter (250-F1) at room temperature. Glass substrates were cleaned ultrasonically in acetone, ethanol and deionized water, successively, then dried in a vacuum oven at about 60°C for 6 h. Products were added into 2 mL ethanol solution and ultrasonicated for 30 min. Then, the suspensions were dipped onto the glass substrates and formed a thin film that was dried naturally. Finally, the film was treated by the methanol solution of 2% (v/v) 1H, 1H, 2H, 2H-perfluorodecyltriethoxysilane (PFOST) at room temperature, followed by drying at 80℃ in vacuum for 1 h. Water droplets (5 μL) were carefully dropped onto the surfaces, and the average value of five measurements obtained at different positions was used as the final contact angle.

3. Results and discussion

3.1. Structural and Elemental analysis

The XRD patterns of the samples were shown in Fig. 1. All diffraction peaks of S9 can be indexed to a pure cubic phase Sb_2O_3 (JCPDS: 43-1071). No impurity peak was detected. The sharp and strong characteristic peaks

suggest that the products were well crystallized. The sample S10 contains a mixture of cubic (JCPDS NO. 43-1071, majority) and orthorhombic (JCPDS NO. 11-0689, minor) crystalline phases. When the initial pH value was increased to 11, all peaks of the obtained sample in the XRD pattern could be well indexed to orthorhombic phase of Sb_2O_3 (JCPDS: 11-689). No impurity peak was observed, which indicates the high phase purity of the as-prepared samples. The above results of different crystal type indicate that the cubic phase Sb_2O_3 completely transformed into orthorhombic phase Sb_2O_3 at pH=11. Therefore, the pH value plays an important role in controlling the crystal type of Sb_2O_3.

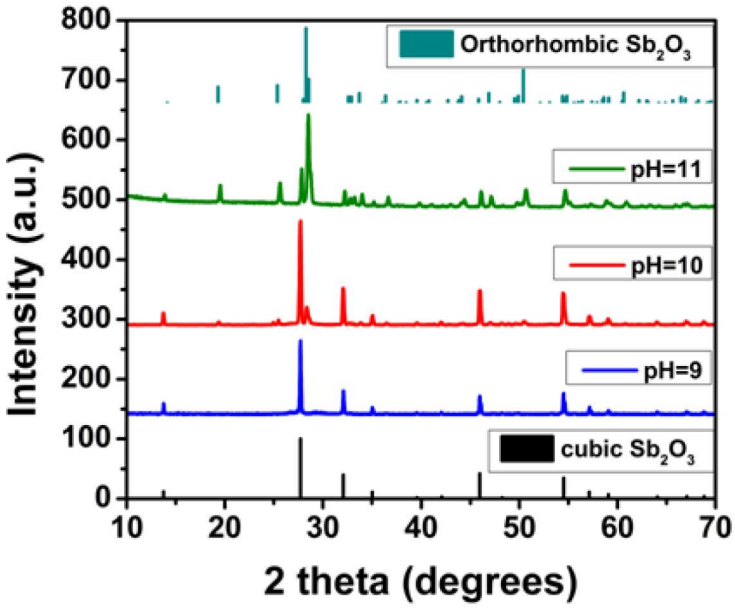

Fig. 1

The elemental composition and electronic states of Sb_2O_3 (S9) powder was investigated by XPS analysis. Figure 2a shows the general XPS survey of the products, where the peaks of Sb, O, and C were found. The Sb 3d 3/2 and

Sb 3d 5/2 binding energies (539.59 and 529.98 eV, respectively) are solely attributed to the presence of Sb^{3+} cations from Sb_2O_3 (Fig. 2b). The peak at 530.06 eV corresponds to the O 1s binding energy (Fig. 2c). The above results further confirmed the formation of Sb_2O_3 and high purity of the product.

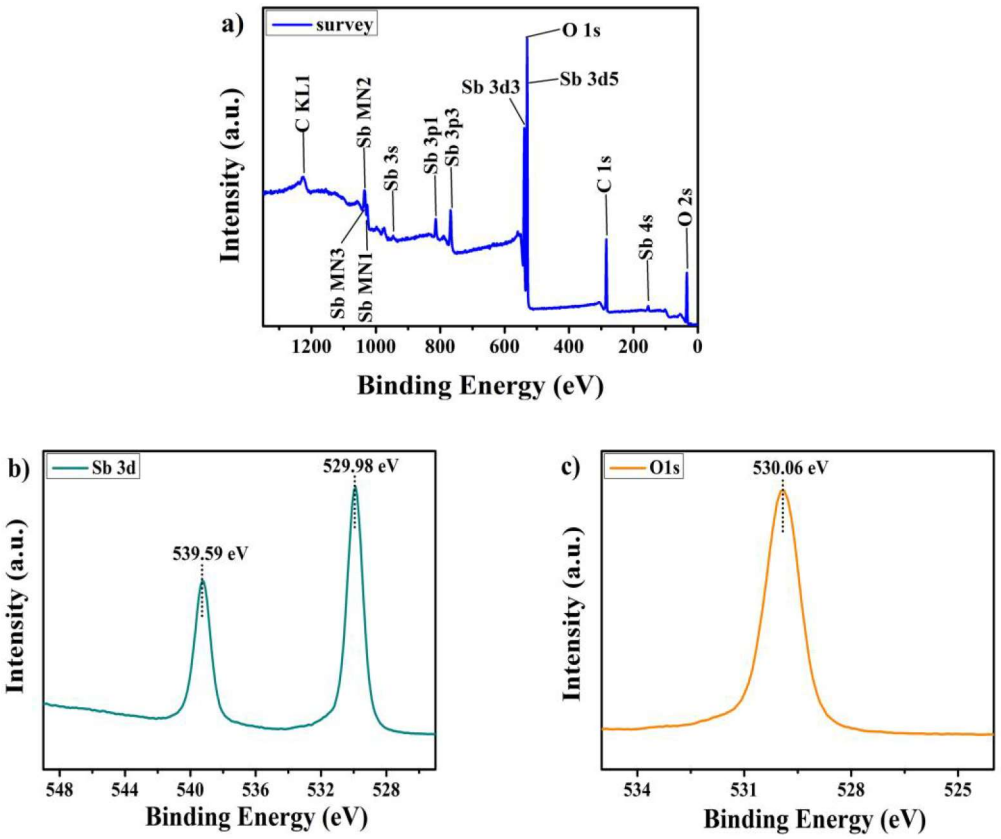

Fig. 2

3.2. Morphology analysis

Morphologies of the products were investigated by SEM. The SEM images of Sb_2O_3 powders prepared via the solvothermal method at different pH values is shown in Fig. 3. It is clear that when the synthesis pH value was tuned to 9, the obtained products consist of a large quantity of Sb_2O_3 octahedron microcrystals at good dispersions. In Fig. 3d, the

high-magnification SEM image shows that these regular octahedral microcrystals have typical edges. The particle width is about 1 μm from one edge to another. As shown in Fig. 3b and Fig. 3e, sample S10 was composed of octahedron microcrystals and a few microspindles. The morphology is quite different from that prepared at pH=11 as shown in Fig. 3c and Fig. 3f. In Fig. 3c, the sample is composed of particles with spindle-like structures, which is uniform with monodispersed size distribution. The magnified SEM image in Fig. 3f shows the edge length is about 5μm and the average diameter is 3 μm. Moreover, the surface of the sample is very rough, which indicates that the microspindles are composed of many smaller homogeneous nanoparticles. These results reveal that the pH value during preparations has a significant influence on the size and morphology of the final products.

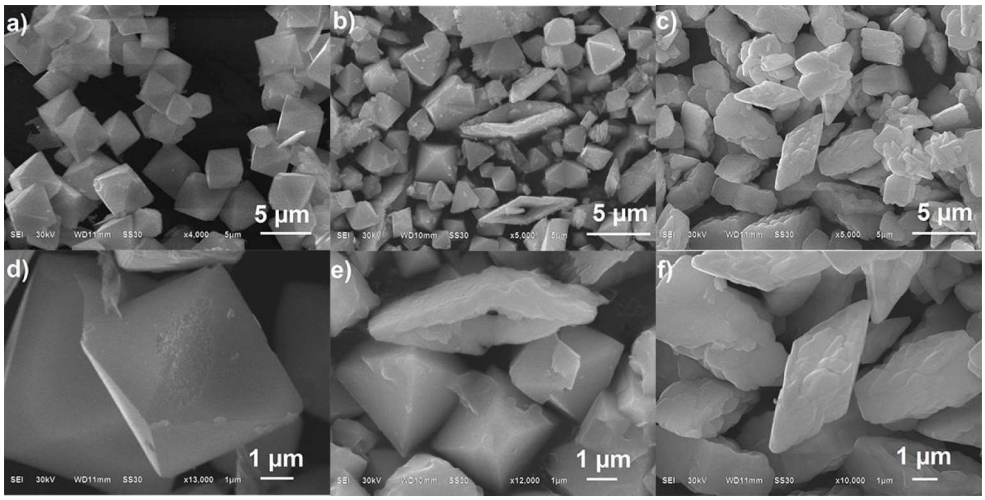

Fig. 3

To explore the shape developing process of Sb_2O_3 octahedron microcrystals, samples prepared at different reaction time were characterized through SEM observation. Fig. 4a exhibits SEM image of the Sb_2O_3 sample

obtained after the reaction was conducted for 12 h. The sample S1 was composed of irregular nanoplates and a small quantity of quadrilateral microcrystals. Besides, the truncated octahedron microcrystals were observed. When the reaction time increased to 24 h, the obtained products were mainly consisted of octahedron microcrystals (Fig. 4b). As the reaction time was further prolonged to 48h, the octahedron microcrystals were completely disappeared and were broken into nanoplates (Fig. 4c). This suggests that the structure of Sb_2O_3 octahedron microcrystals were destroyed when the reaction time was too long.

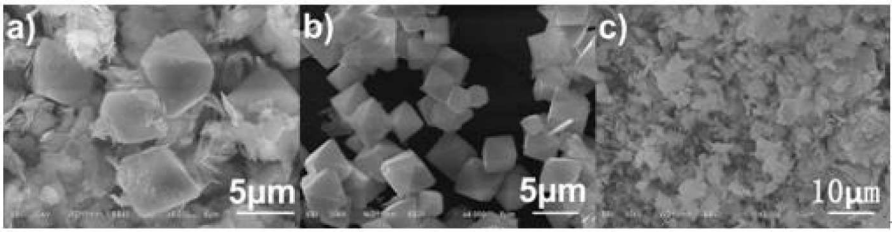

Fig. 4

To study the impact of reaction time on the formation mechanism of Sb_2O_3 microspindles, we investigated the products by changing the solvothermal time. Fig. 5 depicts the morphologies of the products synthesized at 12, 24 and 48 h, respectively. The products prepared at 12h (S3) are obviously spindle-like nanoparticles in the figure. Interestingly, there are some nanoplates distributing among the spindle-like nanoparticles, which are possibly the primary ‘building brick’ nanoparticles of Sb_2O_3 microspindles. Besides, the surface of spindle shape is relatively smooth. Upon further prolonging the reaction time to 24 h, homogeneous and monodispersed spindle-like products

were formed, while relative smooth surface became rough. For an even longer reaction time of 48 h, the product S4 was composed of flower-like structures due to probable self-assemblies of the spindle-like nanoparticles. The above morphology evolution indicates that reaction time plays a key role in determining the shape of orthorhombic Sb_2O_3.

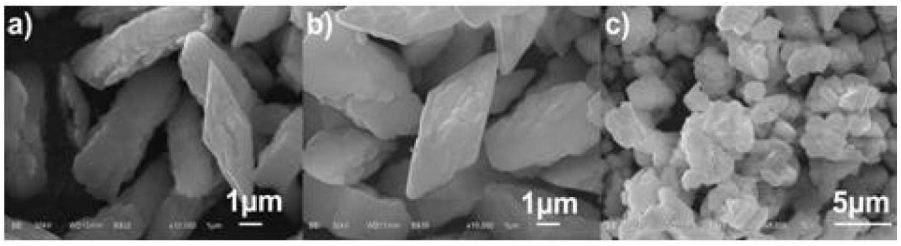

Fig. 5

3.3. Reaction mechanism

Based on the above results, we propose a possible reaction mechanism for the formation of Sb_2O_3 microcrystals. In the first step, the hydrolysis of anhydrous $SbCl_3$ is restrained by the weak interaction between Sb^{3+} and CH_3CH_2OH. Then, with the adding of NaOH solution, $[Sb\cdots CH_3CH_2OH]^{3+}$ can react with OH^-. This leads to the generation of milky $Sb(OH)_3$ precipitates. In hydrothermal process, the $Sb(OH)_3$ precursor can be oxidized in the condition of high pressure and temperature, leading to nucleation of Sb_2O_3 particles. Finally, the Sb_2O_3 particles are aggregated and self-assembled to Sb_2O_3 microcrystals according to Ostwald ripening process. To sum up, the reaction mechanism can be described as follows:

$$Sb^{3+} + CH_3CH_2OH \leftrightarrow [Sb \bullet\ \bullet\ \bullet\ CH_3CH_2OH]^{3+} \quad (1)$$

$$[Sb \bullet\ \bullet\ \bullet\ CH_3CH_2OH]^{3+} + 3NaOH \leftrightarrow Sb(OH)_3 + CH_3CH_2OH + 3Na^+ \quad (2)$$

$$4Sb(OH)_3 + 3O_2 \rightarrow 2Sb_2O_3 + 12OH^- \quad (3)$$

3.4. Influence of $Na_2WO_4 \cdot 2H_2O$

To investigate the impact of $Na_2WO_4 \cdot 2H_2O$ on final morphology of products, the Sb_2O_3 powders were also synthesized in the absence of Na_2WO_4 at different pH values. Fig.6a shows the SEM image of the product synthesized at pH=9. The Sb_2O_3 were square nanoparticles and some irregular particles. Besides, the irregular nanoparticles were obtained in the absence of $Na_2WO_4 \cdot 2H_2O$ for sample S6 (Fig. 6b). Hence, the WO_4^{2-} is very important in the formation process of Sb_2O_3 microcrystals. Indeed, there are many reports on the morphological control via inorganic salts. These inorganic salts can be absorbed on a specific crystal facet and selectively etch certain crystal plane, resulting in specific morphology of the products [35-37]. For example, Ha *et al* found that three distinct gold nanostructures were produced by solely controlling the content of halide ions [35]. In 2010, Niu *et. al* reported that a series of palladium nanocrystals with varying shapes were obtained through manipulation of the concentration of KI [36]. Additionally, different anions could be adsorbed on the surface of the nuclei, which result in the formation of Fe_2O_3 solid urchin-like structures [37]. Similarly, in this work, the anions WO_4^{2-} and OH^- were probably adsorbed at a specific crystal plane of Sb_2O_3 through electrostatic interaction, which decelerated the growth rate of Sb_2O_3 crystal nucleation and prevents the growth of a specific crystal plane of Sb_2O_3.

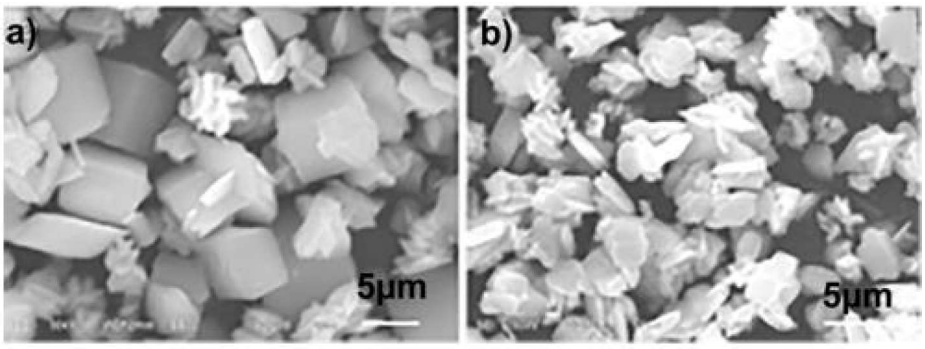

Fig. 6

3.5. Formation mechanism of the Sb_2O_3 microcrystals

Based on the morphology evolution and Ostwald ripening mechanism, a possible formation mechanism of the Sb_2O_3 octahedron microcrystals has been proposed and illustrated as Scheme 1. The whole process includes nucleation, growth, and oriented attachment. At the first step, Sb_2O_3 nanoparticles self-aggregate and grow into nanoplates through dissolution and recrystallization (Ostwald ripening) following the well-known Gibbs-Thomson law [38]. Studies showed that the selective adsorption of ions in solution on different crystal faces will make the nanoparticles grow into various shapes by controlling the growth rates along different crystal directions [39]. At the growth stage, when the pH value is 9, adsorption of OH^- and WO_4^{2-} ions plays a crucial role in guiding the Sb_2O_3 nanoplates. This results in the formation of intermediate diamond-shaped structure. However, when the initial pH value is tuned to 11, more OH^- ions were adsorbed on Sb_2O_3 nanoplates, as confirmed by the SEM image (Fig. 4 and Fig. 5).

To conclude, the formation process of Sb_2O_3 octahedron (microspindles) can be divided into three stages as following. The first stage refers to an initial

formation of Sb_2O_3 nanoplates. In the second stage, formation of intermediate structure is accompanied with the adsorption of different amount of OH^- ions. At the final stage, the octahedrons (spindle-like structures) are formed with the proceeding of the reaction [38, 40].

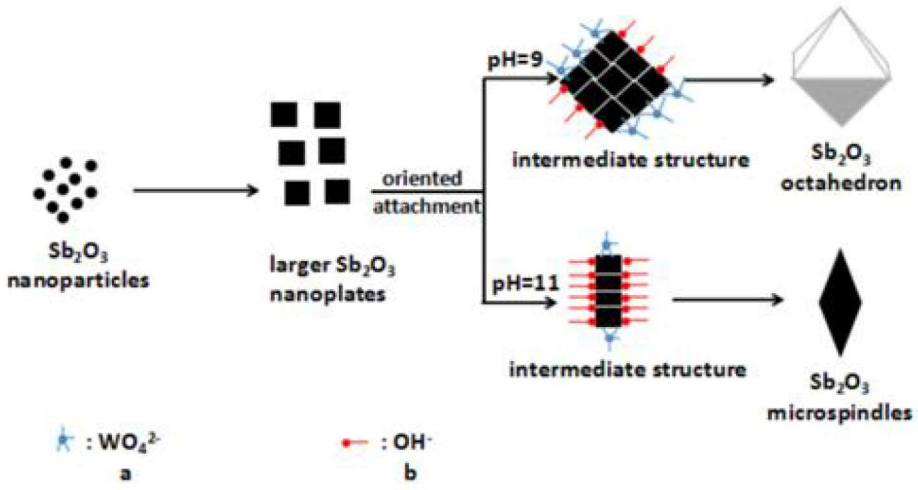

Scheme 1

3.6. CA measurements

Fig.7 shows the surface wettability tests for Sb_2O_3 crystals with different types. The superhydrophobic surface was prepared via a facile dip-coating method. In Fig. 7a, a value of 141.7° is determined to the contact angle of water droplets on the hydrophobic surface of the cubic phase Sb_2O_3 (S9). The water droplets stick to the surface even when it was turned upside down, as shown in Fig. 8 (a) and (b). Modified by PFOST, the CA of water increased to 159.8° (Fig. 7b), exhibiting an excellent superhydrophobic property. The shape of water droplet on the film surface is spherical. The water droplet is not able to stick to the cubic phase Sb_2O_3 surface but rolls off easily, indicating low adhesive force of cubic Sb_2O_3

modified by PFOST. This is attributed to the existence of PFOST on the surface lowers the surface free energy. Fig. 7c shows the contact angles of water droplets on orthorhombic Sb_2O_3 film (S11), where the CA value was 134.5º. Compared with the cubic Sb_2O_3 films, the CA value of orthorhombic Sb_2O_3 film is smaller due to a different surface morphology. Similarly, the orthorhombic Sb_2O_3 film exhibits strong adhesive force (see Fig 8(c) and (d)). After modification of PFOST, the CA of water increased to 155.7° (Fig.7d).

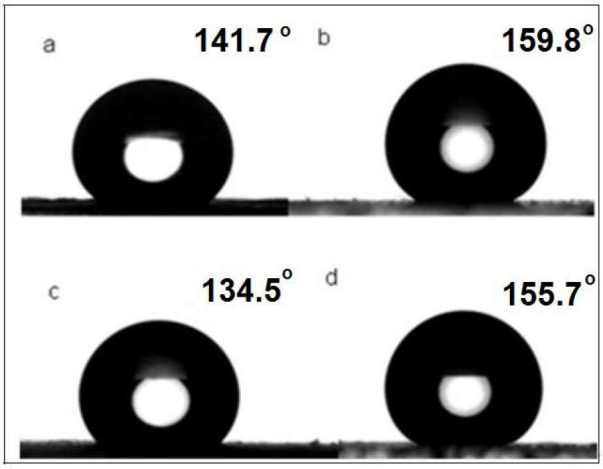

Fig. 7

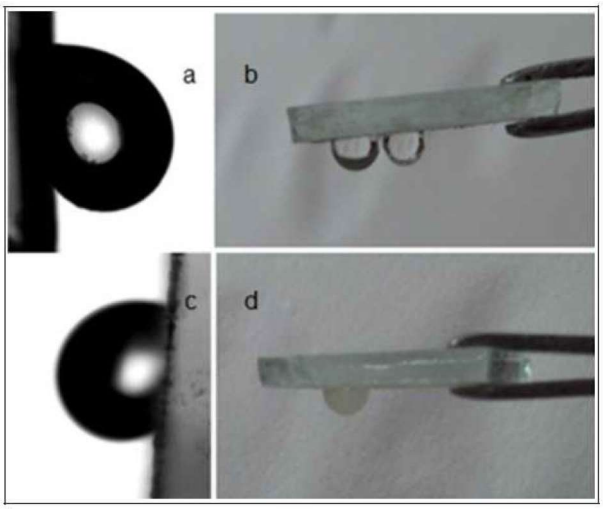

Fig. 8

The experimental results show that the wetting state of Sb_2O_3 film has been obviously changed and transferred to other states. As reported in Ref. [38], the transition could be induced between Cassie and Wenzel configurations under various disturbances from the environment. In this report, the wetting state is changed after modifying by PFOST. A schematic drawing of the regime was depicted in Fig. 9. Without being modified by the PFOST, the Sb_2O_3 film possesses high adhesive properties and is in Wenzel's state. In this case, the water droplet is pinned on the surface, leading to a high CA hysteresis and the generation of a high adhesive force [41]. When the Sb_2O_3 film was modified by PFOST, the wetting state was transferred into Cassie's state. In this state, the water droplets float on the film and can roll off easily from the solid Sb_2O_3 surface film due to air trapped between water droplets and substrates.

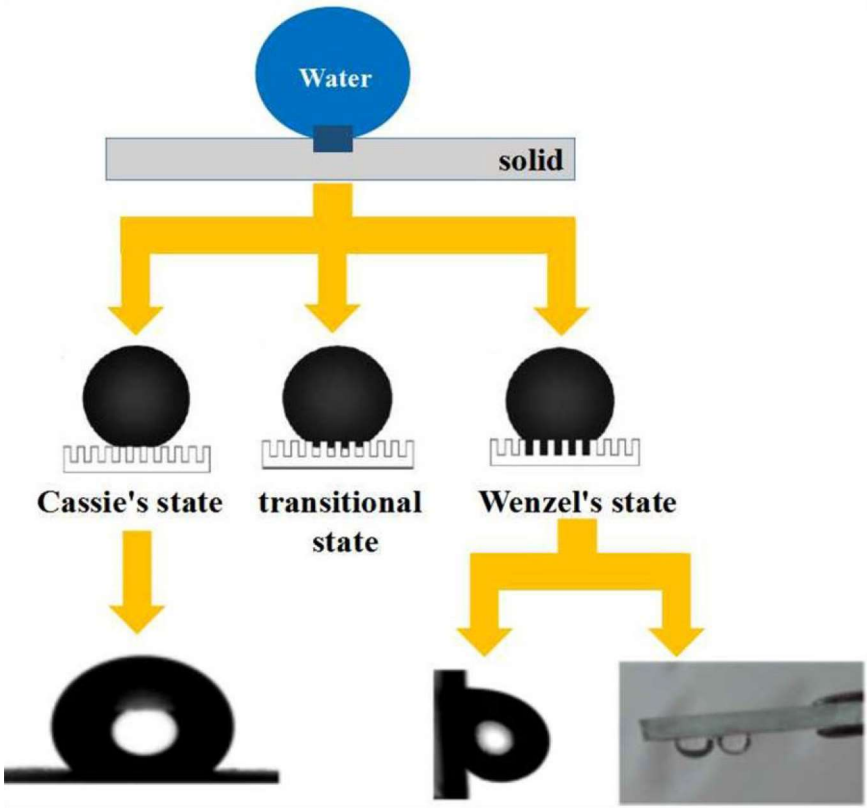

Fig. 9

It is necessary to investigate the wettability of corrosive liquids on the superhydrophobic surface. Fig. 10 shows the relationship between pH values of water droplets and the contact angles on the as-synthesized porous superhydrophobic surface. In Fig. 10a, the contact angles on the PFOTS-treated surface (S9) range from about 152.2° to 159.4° when the pH varied from 3 to 13. Only when the pH value decreased to 1, did the contact angle show a larger fluctuation in the value but still reached about 146.4°. As for sample S11, the fluctuation of the CA with pH is similar to that of the S9 surface. The CA remained in the range of 150.4°-153.4° when the pH increased from 3 to 13. The contact angle decreased to 144.5° when pH =1.

The above results indicated that the superhydrophobic Sb_2O_3 films possess excellent anticorrosion properties against both strong acid and alkali.

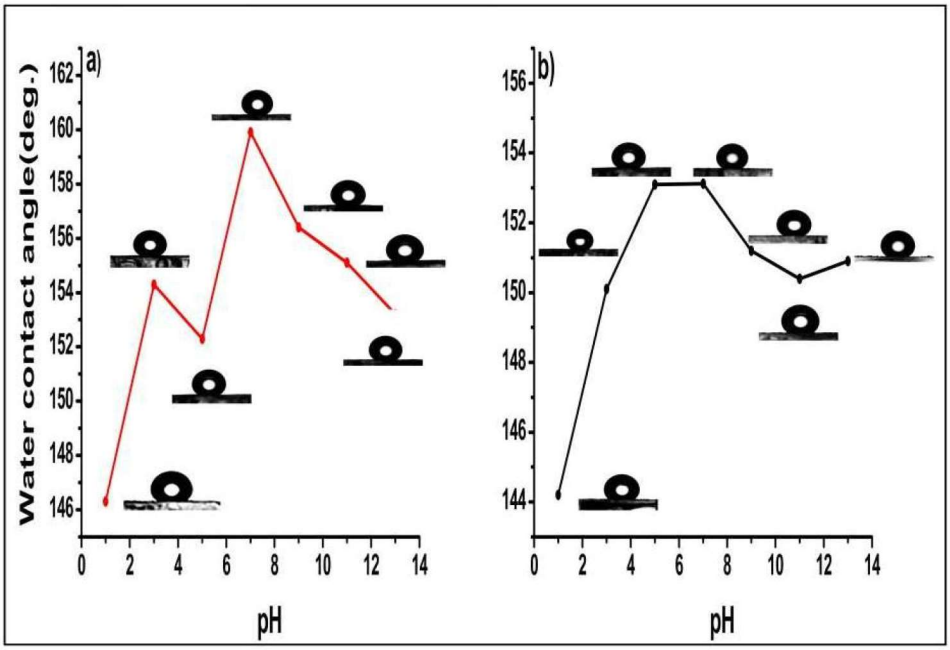

Fig.10

Moreover, the tolerability of Sb_2O_3 film modified by PFOST was also studied. When 5 wt% aqueous solution of NaCl was dripped onto the film, the static CAs of S9 film and S11 films modified by PFOST are 159.4° and 162.4°, respectively (Fig.11). Thus, it is speculated that the corrosion reaction of a 5 wt% aqueous solution of NaCl has little impact on the superhydrophobic surface formed by Sb_2O_3 samples.

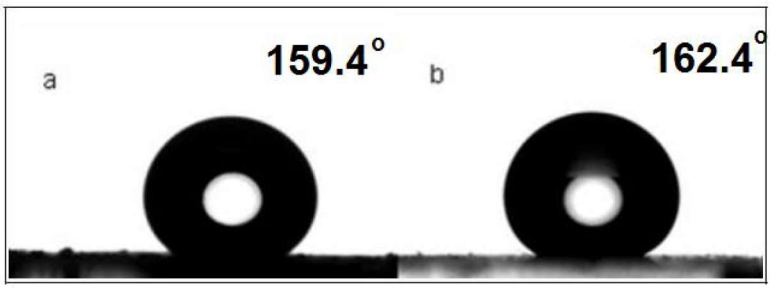

Fig.11

In order to figure out the role of Sb_2O_3 microcrystals on the surface wettability, we also provided the CA of the film only coated by PFOST. As can be seen from Figure 12, the CA of the film is 93.5°, demonstrating that the existence of Sb_2O_3 microcrystals is the key factor to the superhydrophobic surfaces.

Fig.12

4. Conclusions

In summary, cubic Sb_2O_3 octahedra and orthorhombic Sb_2O_3 microspindles have been successfully synthesized by the solvothermal method. The pH values and reaction time strongly affect the morphology, size and crystal phase of products. Possible formation mechanisms for different microstructures are proposed based on the experimental results. Surface coated with Sb_2O_3 show excellent superhydrophobic property and excellent anticorrosion in acidic and basic circumstances.

Acknowledgements

The authors acknowledge the financial support of Scientific Research Fund of Hunan Provincial Education Department, China (16B253), the Open Project Program of State Key Laboratory of Structural Chemistry, China (No. 20150018) and Hunan 2011 Collaborative Innovation Center of Chemical Engineering & Technology with Environmental Benignity and Effective Resource Utilization and the National Natural Science Foundation of China (21343008; 21601149), Oulu University Strategic Grant, and EU Regional Development Fund and Council of Oulu Region. T. Li acknowledges Oulu University Short-term International Research Visit grant during his stay in Finland. Authors also thanks X. Shi for his helps in language improvements.

References

1 Z.X. She, Q. Li, Z.W. Wang, Novel method for controllable fabrication of a superhydrophobicCuO surface on AZ91D magnesium alloy, ACS Appl. Mater. & Inter. 4 (2012) 4348−4356.

2 D. NystrÖm, J. Lindqvist, E. Östmark, Superhydrophobic and self-cleaning bio-fiber surfaces via ATRP and subsequent postfunctionalization,ACS Appl. Mater. & Inter. 1 (2009) 816-823.

3 M. Jönsson-Niedziółka, F. Lapierre, Y. Coffinier, EWOD driven cleaning of bioparticles on hydrophobic and superhydrophobic surfaces, Lab on a chip 11 (2011) 490–496.

4S. Liu, J.F. Ou, Z.P. Li, Layer-by-layer assembly and tribological property of multilayer ultrathin films constructed by modified graphene sheets and polyethyleneimine,Appl.Surf.Sci.258 (2012)2231-2236.

5 J.F.Ou, W.H. Hu, M.S.Xue, One-Step solution immersion process to fabricate superhydrophobic surfaces on light alloys,ACS Appl. Mater. & Inter. 5, (2013) 9867-9871.

6Y. Chen, G. Ou, F. Li, T. H. Li, A facile hydrothermal process to synthesize $Ba_{12}F_{19}Cl_5$ with different morphology and their superhydrophobic property, J. Fluorine Chem. 175 (2015) 121-124.

7 L.B. Boinovich, S.V. Gnedenkov, D.A. Alpysbaeva, Corrosion resistance of composite coatings on low-carbon steel containing hydrophobic and superhydrophobic layers in combination with oxide sublayers, Corros. Sci. 55 (2012) 238-245.

8 P. Guo, Y.M. Zheng, M.X. Wen, Icephobic/Anti-Icing properties of micro/nanostructured surfaces, Adv. Mat. 24 (2012) 2642-2648.

9 N. Saleema, D. K. Sarkar, D. Gallant, Chemical nature of superhydrophobic aluminum alloy surfaces produced via a one-step process using fluoroalkyl-silane in a base medium, ACS Appl. Mater. & Inter. 3 (2011) 4775−4781.

10 Z.J. Han, B.K. Tay, C.M. Tan, Electrowetting control of Cassie-to-Wenzel transitions in superhydrophobic carbon nanotube-based nanocomposites, ACS Nano 3 (2009) 3031-3036.

11 Z. Burton, B. Bhushan, Surface characterization and adhesion and friction properties of hydrophobic leaf surfaces, Ultramicroscopy 106 (2006) 709-719.

12 W. Li, A. Amirfazli, A thermodynamic approach for determining the contact angle hysteresis for superhydrophobic surfaces, J. Colloid Interf. Sci. 292 (2005) 195-201.

13 X.Y. Song, J. Zhai, Y.L. Wang, Fabrication of superhydrophobic surfaces by self-assembly and their water-adhesion properties, J. Phys. Chem. B 109 (2005) 4048-4052.

14 L. Feng, Y.N. Zhang, J.M. Xi, Petal effect: A superhydrophobic state with high adhesive force, Langmuir 24 (2008) 4114-4119.

15 X. Hong, X.f. Gao, L. Jiang, Application of superhydrophobic surface with high adhesive force in no lost transport of superparamagnetic microdroplet, J. Am. Chem. Soc. 129 (2007) 1478-1479.

16 M.H. Jin, X.J. Feng, L. Feng, Superhydrophobic aligned polystyrene nanotube films with high adhesive force, Adv. Mat. 17 (2005) 1977-1981.

17 A. Winkleman, G. Gotesman, A. Yoffe, Immobilizing a drop of water: Fabricating highly hydrophobic surfaces that pin water droplets, Nano Lett. 8 (2008) 1241-1245.

18 M. Callies, D. Quéré, On water repellency, Soft Matter 1 (2005) 55-61.

19 X.H. Xu, Z.Z. Zhang, J. Yang, Study on the superhydrophobic poly(methyl methacrylate)/silver thiolate composite coating with absorption of UVA light, Colloids and Surfaces A: Physicochem. Eng. Aspects 355 (2010) 163-166.

20. G.M. Gong, J.T. Wu, X. Jin, L. Jiang, Adhesion Tuning at Superhydrophobic States: From Petal Effect to Lotus Effect, Macromol. Mater. Eng. 300 (2015) 1057-1062.

21. L. Feng, Y. Zhang, J. Xi, Y. Zhu, N. Wang, F. Xia, Jiang, L.Petal effect: a superhydrophobic state with high adhesive force, Langmuir 24 (2008) 4114–4119.

22. M. H. Jin, X. J. Feng, L. Feng, T. L. Sun, J. Zhai, T. J. Li, L. Jiang, Superhydrophobic aligned polystyrene nanotube films with high adhesive force, Adv. Mater. 17 (2005), 1977–1981.

23 J.J. Tang, Y. Wang, Z. Jiao, Self-assembly nanostructures of one-dimensional antimony oxide and oxychloride, Mater. Lett. 63 (2009) 1481-1484.

24 A.H. Abdullaha, N.H.M. Noora, I. Ramli, Effect of precipitation route on the properties of antimony trioxide, Mater. Chem. Phys. 111 (2008) 201-204.

25 Z.T. Deng, D. Chen, F.Q. Tang, Orientated attachment assisted self-assembly of Sb_2O_3nanorods and nanowires: end-to-end versus side-by-side, J. Phys. Chem. C 111 (2007) 5325-5330.

26 D.B. Wang, Y.H. Zhou, C.X. Song, Phase and morphology controllable synthesis of Sb_2O_3 microcrystals, J. Cryst. Growth 311 (2009) 3948-3953.

27 L. Li, Y.X. Zhang, X.S. Fang, Sb_2O_3nanobelt networks for excellent visible-light-range photodetectors, Nanotechnology 22 (2011) 165704.

28 L. Guo, Z.H. Wu, T. Liu, Synthesis of novel Sb_2O_3 and Sb_2O_5nanorods, Chem. Phys. Lett. 318 (2000) 49-52.

29 H.S. Chin, K.Y. Cheong, K.A. Razak, Controlled synthesis of Sb_2O_3 nanoparticles by chemical reducing method in ethylene glycol, J. Nanopart. Res. 13 (2011) 2807-2818.

30 Z.T. Deng, F.Q. Tang, D. Chen, A simple solution route to single-crystalline Sb_2O_3 nanowires with rectangular cross sections, J. Phys. Chem. B 110 (2006) 18225-18230.

31 Y.X. Zhang, G.H. Li, J. Zhang, Shape-controlled growth of one-dimensional Sb_2O_3 nanomaterials, Nanotechnology 15 (2004) 762-765.

32 K. Kaviyarasu, D. Sajan, P.A. Devarajan, A rapid and versatile method for solvothermal synthesis of Sb_2O_3 nanocrystals under mild conditions, Appl. Nanosci. 3 (2013) 529-533.

33 Y.X. Zhang, G.H. Li, L. Zhang, Growth of Sb_2O_3 nanotubes via a simple surfactant-assisted solvothermal process, Chem. Lett. 33 (2004) 334-335.

34 Q.R. Zhao, X.J. Zhang, Q. Yang, One-step synthesis of Sb_2O_3 broom-like belts with controllable morphology, Can. J. Chem. 83, (2005) 1093-1097.

32 S.Y. Zeng, R.F. Tang, H.F. Su, Mono-disperse $CaWO_4$ microsphere with hierarchical structures: room temperature synthesis and its optical properties, NANO: Brief Reports and Reviews 11 (2016) 1650039.

33 M.J. Siegfried, K.S. Choi, Elucidating the effect of additives on the growth and stability of Cu_2O surfaces via shape transformation of pre-grown crystals, J. Am. Chem. Soc. 128 (2006) 10356-10357.

34 Y. Yan, Y.F. Wu, Y.T. Yan, W.S. Guan, W.D. Shi, Multispectroscopic (FTIR, XPS, and TOFMS-TPD) investigation of the core-shell bonding in sonochemically prepared aluminum nanoparticles capped with oleic acid, J. Phys. Chem. C 117 (2013) 20017-20028.

35 H. H. Tai, A. H. Koo, B. H. Chung, Shape-controlled syntheses of gold nanoprisms and nanorods influenced by specific adsorption of halide ions, J. Phys. Chem. C, 111 (2007), 1123-1130.

36 W.X. Niu, L. Zhang, G.B. Xu, Shape-Controlled Synthesis of Single-Crystalline Palladium Nanocrystals, ACS Nano 4 (2010) 1987-1996.

37 S.Y. Zeng, K.B. Tang, T.W. Li, Z.H. Liang, Hematite with the Urchinlike Structure: Its Shape-Selective Synthesis, Magnetism, and Enhanced Photocatalytic Performance after TiO_2 Encapsulation, J. Phys. Chem. C 114 (2010) 274-283.

38 W.Q. Cai, J.G. Yu, M. Jaroniec, Templete-free synthesis of hierarchical spindle-like γ-Alumina materials and their adsorption affinity towards organic and inorganic pollutants in water, J. Mater. Chem. 20 (2010) 4587-4594.

39 S.F. Wu, T.M. Liu, W. Zeng, Octahedral cuprous oxide synthesized by hydrothermal method in ethanolamine/distilled water mixed solution, J. Mater. Sci.: Mater. Electron. 25 (2014) 974-980.

40 C.C. Yu, M. Yu, C.X. Li, C.M. Zhang, P.P. Yang, J. Lin, Spindle-like lanthanide orthovanadate nanoparticles: facile synthesis by ultrasonic irradiation, characterization, and luminescent properties, Crystal Growth & Design 9 (2009) 783-791.

41 S.T. Wang, K.S. Liu, X. Yao, L. Jiang, Bioinspired surfaces with superwettability: New insight on theory, design, and applications, Chem. Rev. 115 (2015) 705-709.

Table and Figure captions

Table 1 The synthetic conditions of Sb_2O_3samples.

Fig.1. XRD patterns of the prepared Sb_2O_3 microcrystalline at different pH values.

Fig. 2. (a) Whole XPS spectrum pattern of the Sb_2O_3 (S9), (b) Sb 3d of Sb_2O_3 (S9), (c) O1s of Sb_2O_3 (S9).

Fig. 3. SEM images of the Sb_2O_3 prepared at different pH: (a) and (b) S9, (c) and (d) S10, (e) and (f) S11.

Fig. 4. SEM images of the octahedral Sb_2O_3 prepared at different reaction time: (a) S1 (t = 12 h), (b) S9 (t = 24 h), (c) S2(t = 48 h).

Fig. 5. SEM images of the microspindles Sb_2O_3 prepared at different reaction time: (a) S3 (t = 12 h), (b) S11 (t = 24 h), (c) S4 (t = 48 h).

Fig. 6. SEM images of the Sb_2O_3 prepared in the absent of Na_2WO_4 and different pH: (a) S5 (pH=9), (b) S6 (pH=11).

Fig. 7. The CA value of Sb_2O_3 microcrystalline: (a) and (b) S9 without modification and modified by a methanol solution of 2% (v/v) PFOST. (c) and (d) S11 without modification and modified by a methanol solution of 2% (v/v) PFOST.

Fig. 8. (a) and (b) profile of a water droplet on the S9 film without modification, when set upright and turned upside down,(c) and (d) Profile of a water droplet on the S11 film without modification, when set upright and turned upside down, respectively.

Fig. 9. Schematic illustration of interactions between the water droplets and surfaces: Cassie-Wenzel regime.

Fig. 10. Variation of water contact angle with the different pH values of the dipping water on the (a) Sb_2O_3 film (S9); (b) Sb_2O_3 film (S11) modified by PFOST.

Fig. 11. The tolerability of (a) cubic Sb_2O_3 film (S9) modified by PFOST, (b) orthorhombic Sb_2O_3 film (S11) modified by PFOST in 5 wt% NaCl aqueous solution.

Fig. 12. The CA of the film prepared by PFOST only.

Scheme 1. Possible schematic illustration of the growth process of Sb_2O_3 microcrystals at different pH values.